Finally, the Yarkovsky semimajor axis drift may be important in transporting to the main resonances a large number of bodies around 10 m in radius for which Δa values of ~0.1 AU are expected (Fig. 1C), similar to the distances between the main Kirkwood gaps. These fragments may be removed from the main belt population faster than bodies of other sizes, and in turn this may result into longer collisional lifetimes τ_{dis} for the 100-m objects, which would also become more mobile (*29*). Although a realistic model of the feedback effects between Yarkovsky orbital drift and collisional processing of the asteroid size distribution would be required to assess these effects, we suggest that the Yarkovsky mobility mechanism may provide a plausible explanation for the observed overabundance of bodies 10 to 100 m in diameter in the near-Earth population (*18*).

References and Notes

1. A. Milani, A. M. Nobili, P. Farinella, *Non-Gravitational Perturbations and Satellite Geodesy* (Hilger, Bristol, UK, 1987).
2. J. A. Burns, P. L. Lamy, S. Soter, *Icarus* **40**, 1 (1979).
3. D. Brouwer and G. M. Clemence, *Methods of Celestial Mechanics* (Academic Press, New York, 1961), chap. 16.
4. C. R. Chapman *et al.*, in *Asteroids II*, R. P. Binzel, T. Gehrels, M. S. Matthews, Eds. (Univ. of Arizona Press, Tucson, AZ, 1989), pp. 386–415.
5. V. Zappalà *et al.*, *Icarus* **116**, 291 (1995).
6. E. J. Öpik, *Proc. R. Irish Acad.* **54**, 165 (1951); V. V. Radzievskii, *Astron. Zh.* **29**, 162 (1952); C. Peterson, *Icarus* **29**, 91 (1976); G. Afonso, R. S. Gomes, M. A. Florczak, *Planet. Space Sci.* **43**, 787 (1995).
7. D. P. Rubincam, *J. Geophys. Res.* **92**, 1287 (1987); P. Farinella and D. Vokrouhlický, *Planet. Space Sci.* **44**, 1551 (1996); V. J. Slabinski, *Celest. Mech. Dyn. Astron.* **66**, 131 (1997).
8. D. P. Rubincam, *J. Geophys. Res.* **100**, 1585 (1995).
9. P. Farinella, D. Vokrouhlický, W. K. Hartmann, *Icarus* **132**, 378 (1998).
10. D. Vokrouhlický and P. Farinella, *Astron. Astrophys.* **335**, 351 (1998); W. K. Hartmann *et al.*, *Meteorit. Planet. Sci.*, in press.
11. For the seasonal effect, see D. P. Rubincam, *J. Geophys. Res.* **103**, 1725 (1998); D. Vokrouhlický and P. Farinella, *Astron. J.* **116**, 2032 (1998); for the diurnal effect, see D. Vokrouhlický, *Astron. Astrophys.* **335**, 1093 (1998).
12. D. R. Davis *et al.*, in (*4*), pp. 805–826; P. Farinella *et al.*, *Astron. Astrophys.* **257**, 329 (1992); R. Greenberg *et al.*, *Icarus* **107**, 84 (1994); D. R. Davis *et al.*, *ibid.* **120**, 220 (1996).
13. Such a relation is roughly in agreement with the results of laboratory experiments on the catastrophic fragmentation of bodies ~20 cm in diameter [I. Giblin *et al.*, *Icarus* **110**, 203 (1994); *ibid.* **134**, 77 (1998)], with the inferred rotation rate of the Lost City fireball [3.3 s for a diameter of ~0.5 m; see Z. Ceplecha, *Astron. Astrophys.* **311**, 329 (1992)], with the ~10 min spin rate of the small NEA 1998 KY$_{26}$ (several tens of meters across) [P. Pravec and L. Sarounova, *IAU Circ.* **6941**, 2 (1998)], and with the typical spin periods of several hours for small main-belt asteroids [R. P. Binzel *et al.*, in (*4*), pp. 416–441].
14. At each time step Δt we computed a spin axis reorientation probability $P = 1 - \exp(-\Delta t / \tau_{rot})$, where $\tau_{rot} = 15.0 \times (R/1\ \mathrm{m})^{1/2}$ My for stony bodies and $\tau_{rot} = 37.5 \times (R/1\ \mathrm{m})^{1/2}$ My for metal-rich bodies. We then used a Monte Carlo procedure to select the particles to be reoriented. The normalizing coefficient of the τ_{rot} formula is in agreement with our assumed relation between spin rate and size, and is about 4.5 times the value adopted in (*9*). This results in a diurnal Yarkovsky drift about 1.7 times faster. The uncertainty of the diurnal drift related to our limited knowledge of τ_{rot} is about a factor of 2, on the same order as those associated with the collisional lifetime and the thermal parameters.
15. M. W. Caffee *et al.*, in *Meteorites and the Early Solar System*, J. F. Kerridge and M. S. Matthews, Eds. (Univ. of Arizona Press, Tucson, AZ, 1988), pp. 205–245; K. Marti and T. Graf, *Annu. Rev. Earth Planet. Sci.* **20**, 221 (1992). As explained in (*9*), this relation between τ_{dis} and R is also consistent with the steady-state size distribution of small asteroid fragments predicted in (*30*).
16. K. Yomogida and T. Matsui, *J. Geophys. Res.* **88**, 9513 (1983).
17. For the upper layer of the lunar regolith, a typical value of 0.0015 W/(m·K) has been reported [M. G. Langseth, S. J. Keihm, J. L. Chute, in *Apollo 17—Preliminary Science Report*, NASA SP-330 (1973)]. Measurements for porous or particulate stony materials have been performed [A. E. Wechsler, P. E. Glaser, A. D. Little, J. A. Fountain, in *Thermal Characteristics of the Moon*, J. W. Lucas, Ed. (MIT Press, Cambridge, MA, 1972), pp. 215–242; see also M. A. Presley and P. R. Christensen, *J. Geophys. Res.* **102**, 6551 (1997)].
18. D. P. Rabinowitz, *Astrophys. J.* **407**, 412 (1993); *Icarus* **111**, 364 (1994); *ibid.* **130**, 287 (1998); P. Farinella and M. Menichella, *Planet. Space Sci.* **46**, 303 (1998).
19. G. W. Wetherill, *Meteoritics* **15**, 386 (1980); G. F. Herzog *et al.*, *Meteorit. Planet. Sci.* **32**, 413 (1997).
20. P. Farinella *et al.*, *Nature* **371**, 314 (1994); F. Migliorini *et al.*, *Meteorit. Planet. Sci.* **32**, 903 (1997); B. J. Gladman *et al.*, *Science* **277**, 197 (1997).
21. F. Migliorini *et al.*, *Science* **281**, 2022 (1998).
22. A. Morbidelli and D. Nesvorný, *Icarus*, in press.
23. M. Menichella *et al.*, *Earth Moon Planets* **72**, 133 (1996).
24. A. Morbidelli and B. J. Gladman, *Meteorit. Planet. Sci.* **33**, 999 (1998).
25. T. Nakamura, in *Seventy-Five Years of Hirayama Asteroid Families*, Y. Kozai, R. P. Binzel, T. Hirayama, Eds. (Astronomical Society of the Pacific, San Francisco, 1994), Conference Series vol. 63, pp. 52–61.
26. Such a relation has been reported [A. M. Nakamura and A. Fujiwara, *Icarus* **92**, 132 (1991); ———, T. Kadono, *Planet. Space Sci.* **42**, 1043 (1994)]. On the other hand, recent experimental results [I. Giblin, *ibid.* **46**, 921 (1998)] show that the fragment size-velocity correlation is probably weak and dependent on the experimental setup.
27. A. Milani and P. Farinella, *Icarus* **115**, 209 (1995).
28. Z. Knežević, A. Milani, P. Farinella, *Planet. Space Sci.* **45**, 1581 (1998).
29. In Fig. 1, A to C, we did not take into account these feedback effects, and just assumed $\tau_{dis} \propto R^{1/2}$, consistent with the equilibrium size distribution predicted in (*30*) for scale-independent collisional systems. However, if the "Yarkovsky sink" is effective for objects ~10 m in radius, this may introduce a lower-cutoff effect in the size distribution, resulting in a wave-like pattern superimposed on the Dohnanyi power-law size distribution [see A. Campo Bagatin *et al.*, *Planet. Space Sci.* **42**, 1079 (1994)].
30. J. W. Dohnanyi, *J. Geophys. Res.* **74**, 2531 (1969).

16 September 1998; accepted 25 January 1999

Quartzlike Carbon Dioxide: An Optically Nonlinear Extended Solid at High Pressures and Temperatures

V. Iota, C. S. Yoo,* H. Cynn

An extended-solid phase, carbon dioxide phase V (CO_2-V), was synthesized in a diamond anvil cell by laser heating the molecular orthorhombic phase, carbon dioxide phase III, above 40 gigapascals and 1800 kelvin. This new material can be quenched to ambient temperature above 1 gigapascal. The vibration spectrum of CO_2-V is similar to that of the quartz polymorph of silicon dioxide, indicating that it is an extended covalent solid with carbon-oxygen single bonds. This material is also optically nonlinear, generating the second harmonic of a neodymium–yttrium-lithium-fluoride laser at a wavelength of 527 nanometers with a conversion efficiency that is near 0.1 percent.

High pressure alters the nature of chemical bonds, electronic and crystal structures, and thermal and mechanical properties of solids. It has been suggested that simple molecular solids may transform into a polymeric phase before they become metals at high pressure (*1*). Theoretical models and experimental data support this hypothesis, including polymeric forms of N_2 (*1*), CO (*2*), diamond (*3*), β-C_3N_4 (*4*), and symmetric H_2O (*5*). Furthermore, these pressure-induced changes often occur in systematic ways, providing new routes for designing and synthesizing novel materials with advanced optical and mechanical properties. The structures of the N_2 polymer, diamond, and β-C_3N_4 at high pressures, for example, can be viewed as being similar to the assemblages of heavier elements in each periodic group (P, Si, and β-Si_3N_4, respectively) at low pressures.

Carbon dioxide is one of the most abundant volatile materials on Earth. Also, CO_2 crystals (dry ice) are widely used for cooling, and CO_2 is found as clathrates on Mars and other planets (*6*). However, the properties of CO_2 at high pressures are not well understood. Four polymorphs have been suggested for CO_2, but the structures and stability of

---

Lawrence Livermore National Laboratory, University of California, Livermore, CA 94551, USA.

*To whom correspondence should be addressed. E-mail: yoo1@llnl.gov

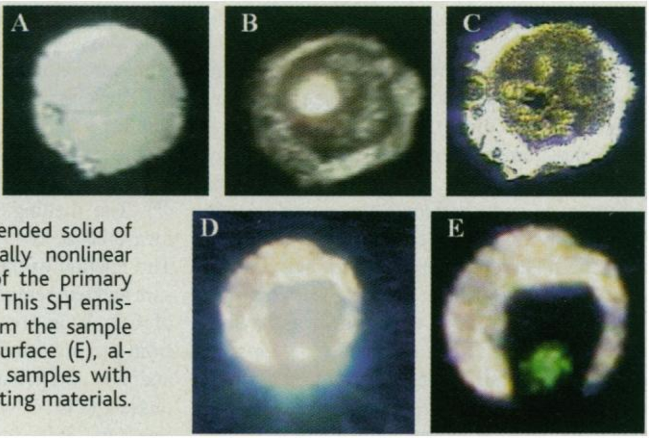

Fig. 1. Microphotographs of CO_2 samples through (**A** through **C**) ruby chips and (**D** and **E**) a Pt foil at 45 GPa before (A), during (B and D), and after several heatings (C and D). After heating (C), the molecular phase, CO_2-III, transformed into a new extended solid of CO_2-V. CO_2-V is an optically nonlinear crystal generating the SH of the primary Nd:YLF laser at 527 nm (E). This SH emission is most easily seen from the sample with a shiny reflecting Pt surface (E), although it is observed in all samples with CO_2-V, regardless of the heating materials.

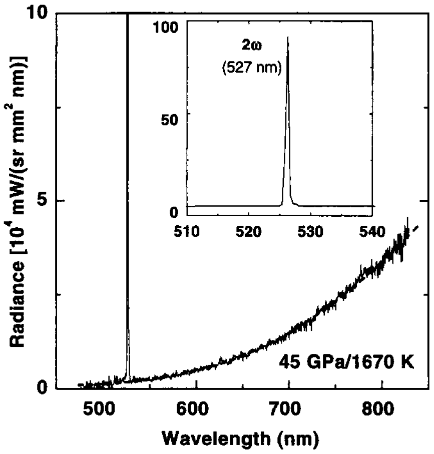

Fig. 2. A typical emission spectrum obtained during the heating of CO_2 at 45 GPa, which shows a broad thermal emission and a sharp emission at 527 nm. The sharp emission is clearly the SH of our Nd:YLF laser (also shown in the inset). The conversion efficiency of this nonlinear process is estimated to be ~0.1%. The gray-body fit of the broad emission (dashed line) gives the sample temperature as 1670 K.

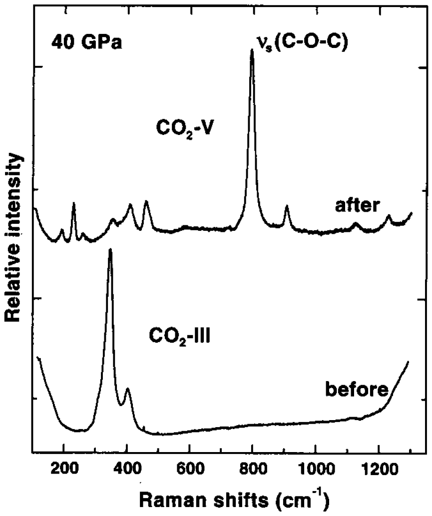

Fig. 3. Raman spectra of CO_2 at 40 GPa (measured before and after heating) show a transformation from a molecular phase of CO_2-III to an extended-solid phase of CO_2-V. The strong band at 790 cm^{-1} after heating is the symmetric stretching mode A_1, ν_s(C–O–C), suggesting that CO_2-V contains C–O single bonds. The spectrum of CO_2-III is broad because of a large pressure gradient in the sample, which indicates an unusually high strength of this phase for a molecular crystal.

these polymorphs have been incompletely characterized (*7*). The strength of CO_2 (the orthorhombic phase III in particular) increases substantially with increasing pressure (*8*), which is unusual for a van der Waals molecular solid. Here, we report the discovery of a new transition from the molecular solid, CO_2 phase III (CO_2-III), to a polymeric form, CO_2-V, whose structure and optical properties are analogous to the quartz polymorph of SiO_2. We suggest that the strength increase in CO_2-III is a precursor to this transition.

Liquid CO_2 was loaded in a diamond anvil cell (DAC), which was contained in a high-pressure vessel by condensing CO_2 gas at −40°C and 10 atm. A few micrometer-sized ruby chips were scattered inside the cell, providing an in situ determination of pressures at several locations of the sample. Samples of CO_2 were indirectly heated by irradiating the ruby chips, a small Pt foil, or a Re gasket with a neodymium–yttrium-lithium-fluoride (Nd:YLF) laser operating in TEM_{00} (transverse electromagnetic) mode at 1054 nm. Approximately 20 experiments were carried out to synthesize CO_2-V, and the results were independent of the materials used for heating. Direct laser heating of the CO_2 was not feasible because of its low absorption at this wavelength. The temperature of the sample was determined by fitting the thermal emission from the heated area to a gray-body radiation formula. Details of the laser-heating experiments were previously described elsewhere (*9*).

Microphotographs (Fig. 1) of the CO_2 samples that were heated through ruby chips and a Pt foil show that CO_2-III transforms into a new translucent CO_2-V within the laser-heated area. The gray-body fit of thermal emission during heating indicates that the initial transformation occurs above 1800 K and is often associated with a high translucent excursion of the intensity of the light (Fig. 1D). The highest temperature attained during the transition was 3400 K. Figures 1E and 2 show strong emission at 527 nm, which corresponds to the second harmonic (SH) of the Nd:YLF laser. The intensity of this sharp SH band at 527 nm depends on how the Nd:YLF output was partitioned between heating and SH generation. The gray-body fit of the broad thermal emission in Fig. 2 indicates that the temperature of the laser-heated area was 1670 K. We estimate the SH conversion efficiency of this new phase to be ~0.1% (*10*). The SH radiation was observed in all 20 samples that underwent the transition, indicating that the frequency-doubling process is inherent to the new phase and does not rely on trace impurities that may be incorporated in the CO_2 lattice during heating. A relatively large pressure drop (up to 5 to 10% of the initial pressure) was also observed after forming CO_2-V by several cycles of laser heating. This suggests that a large volume collapse is associated with the transition. This new phase is metastable over a large pressure range above 1 GPa, at which pressure it transforms back to liquid CO_2 when the DAC is unloaded.

Raman spectra that were obtained before and after the heating of a sample at 40 GPa (Fig. 3) indicate that the orthorhombic molecular CO_2-III transforms to a new extended-solid CO_2-V, whose structure is similar to the quartz or coesite polymorphs of SiO_2. For example, the broad features between 200 and 400 cm^{-1} before heating are characteristic to the orthorhombic CO_2-III (*11*). However, the spectrum (after heating) is different from the vibration characteristics of any known molecular polymorph of CO_2, suggesting that it has a different structure. We assigned the most dominant vibration feature at 790 cm^{-1} to the symmetric stretch of the C–O–C bonds, ν_s(C–O–C). On the basis of the pressure dependence shown in Fig. 4, this mode should be located at 660 cm^{-1} at ambient conditions of pressure and temperature. This frequency of ν_s(C–O–C) was then translated to 398 to 491 cm^{-1} from the ν_s(Si–O–Si) mode in SiO_2 polymorphs, depending on the approximation used in the reduced-mass calculation (*12*). This mass-weighted vibron frequency agrees reasonably well with ν_s(Si–O–Si) frequencies in quartz at 464 cm^{-1} and in coesite at 510 cm^{-1} (*12, 13*). In contrast, the analogous mode of stishovite, a high-pressure polymorph of SiO_2, occurs at 750 cm^{-1} at ambient conditions (*13*), which is a higher frequency than ν_s(C–O–C) at 660 cm^{-1} for CO_2-V. The large pressure-dependent shift of ν_s(C–O–C) (Fig. 4) is also analogous to that of ν_s(Si–O–Si) in the coesite or quartz polymorphs of SiO_2. As previously explained for SiO_2 (*13–15*), the strong shift of ν_s(C–O–C) implies a high compressibility of CO_2-V as a result of a large change of C–O–C angles in this open structure.

Symmetry considerations for SH generation processes provide further evidence that the crystal structure of CO_2-V is quartzlike. Strong SH generation of light has been observed in solid forms of SiO_2 (including crystalline, amorphous, and semiconductor-doped glass) with a conversion efficiency of up to 20% (*16, 17*). The relatively sharp phonons and vibrons of CO_2-V (Fig. 3) imply that CO_2-V is not vitreous; SiO_2 glass is well known as having extremely broad vibration bands (*13*). On the other hand, the SH process is symmetry forbidden in a crystal structure with a center of inversion (*18*). This further excludes the possibility of CO_2-V being a centrosymmetric crystal like coesite or stishovite of SiO_2 (*19, 20*). Therefore, it is possible that the structure of CO_2-V is noncentrosymmetric and quartzlike (*19*).

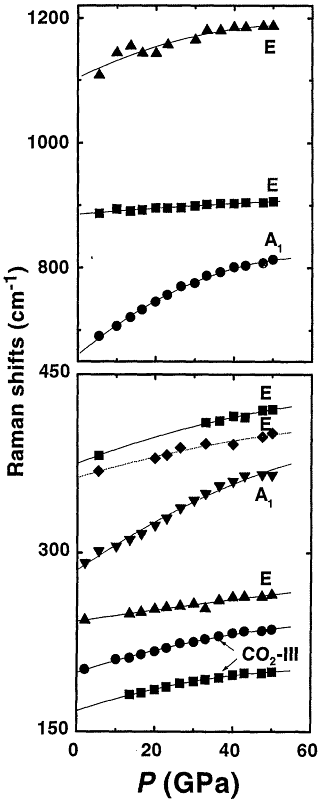

Fig. 4. Pressure (*P*) dependence of various vibrations of a new extended-solid phase of CO_2-V. This new phase is metastable above 1 GPa and ambient temperature. The Raman spectra were obtained during the unloading of quenched samples after laser heating at pressures between 40 and 60 GPa and at temperatures above 1800 K. The symmetry assignment was based on that of the quartz polymorph of SiO_2 in (*13–15*). Two phonon bands below 240 cm^{-1} are probably from those of untransformed CO_2-III. There is a strong pressure-induced shift of the symmetric (A_1) C–O–C stretching mode at 660 cm^{-1} at ambient conditions. A similarly strong pressure dependence was previously observed in the A_1 mode of SiO_2 in quartz and coesite polymorphs and is explained in terms of a large-angle change of the Si–O–Si ring in those open structures of SiO_2 (*13–15*). Curves are labeled as E, doubly degenerated vibrational modes; A_1, symmetric stretching mode; and CO_2-III, untransformed CO_2-III.

The pressure and temperature domains of stability and metastability of CO_2-V are shown in Fig. 5, together with those of other CO_2 polymorphs, which were previously suggested (*7*). The melting line of CO_2 has only been measured at low pressures below 1 GPa (*21*). The relation of the melting line with the pressure and temperature conditions of the synthesis of CO_2-V is not known. CO_2-V forms only from the orthorhombic CO_2-III above 40 GPa and 1800 K. Laser heating of the cubic CO_2 phase I (CO_2-I) or CO_2-III at lower pressures (even to 2800 K) does not yield CO_2-V, indicating that there is a sharp phase boundary between CO_2-III and CO_2-V above 40 GPa. However, this transition appears to be less sensitive to temperature at pressures of up to 60 GPa, which is the maximum pressure that was studied for heating. These observations may imply that the temperature boundary at 1800 K represents a kinetic barrier rather than the thermodynamic phase boundary. The fact that this transition does not occur to 70 GPa at ambient temperature suggests the existence of a large activation barrier in this transition. The metastability of CO_2-V in a large pressure region is also consistent with this conjecture.

Above 40 GPa, CO_2-III supports an extremely large pressure gradient of more than 100 to 200 GPa mm^{-1} (*8*). This pressure gradient is extremely large for a van der Waals solid, indicating that CO_2-III may not be purely molecular but may have strong intermolecular interactions or even relatively weak intermolecular bonding at these pressures. Such weak intermolecular bonding would have two counteracting consequences: (i) Delocalization of electrons in CO_2 molecules would soften the steep repulsive potential and prolong the stability of CO_2-III to pressures well above 40 GPa at ambient temperature; (ii) on the other hand, such an intermolecular coupling in CO_2-III would lower the activation barrier for breaking the strong C-O double bonds, thereby lowering the transition pressure at high temperature.

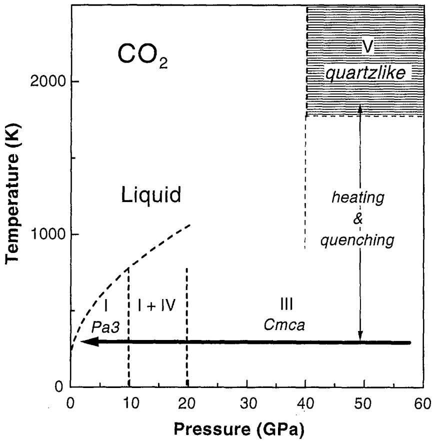

Fig. 5. Pressure and temperature conditions required for the synthesis of CO_2-V, superimposed on the phase diagram of CO_2 that was reproduced from Raman and x-ray measurements in (*7*). The melting line (dashed curve) is the extrapolation of low-pressure values in (*21*). CO_2-V was synthesized by laser heating of CO_2-III above 40 GPa and 1800 K and can be quenched at ambient temperatures above 1 GPa. The vertical dashed lines at 10, 20, and 40 GPa indicate the phase boundaries of CO_2. The horizontal dashed line at 1800 K illustrates the kinetic line for the transformation from CO_2-III to CO_2-V.

References and Notes

1. C. Mailhiot, L. H. Yang, A. K. McMahan, *Phys. Rev. B* **46**, 14419 (1992).
2. S. Bernard, G. L. Chiarotti, S. Scandolo, E. Tosatti, *Phys. Rev. Lett.* **81**, 2092 (1998).
3. F. P. Bundy and J. S. Kasper, *J. Chem. Phys.* **46**, 3437 (1967).
4. A. Y. Liu and M. L. Cohen, *Science* **245**, 841 (1989).
5. A. F. Goncharov, V. V. Struzhkin, M. S. Somayazulu, R. J. Hemley, H. K. Mao, *ibid.* **273**, 218 (1996).
6. S. L. Miller and W. D. Smythe, *ibid.* **170**, 531 (1970); D. Musselwhite and J. Lunine, *J. Geophys. Res.* **100**, 23301 (1995).
7. Four polymorphs of CO_2 have been suggested at high pressures: (i) a cubic *Pa3* phase of CO_2-I below 10 GPa [B. Olinger, *J. Chem. Phys.* **77**, 6255 (1982)], known as dry ice; (ii) a less well-characterized phase of CO_2-II, which has been proposed as occurring between 0.5 and 2.3 GPa [L. Liu, *Nature* **303**, 508 (1983)]; (iii) an orthorhombic *Cmca* phase of CO_2-III [K. Aoki, H. Yamawaki, M. Sakashita, Y. Gotoh, K. Takemura, *Science* **263**, 356 (1994)]; and (iv) a "distorted" phase of CO_2-IV, which has been proposed as occurring between the stability fields of CO_2-I and CO_2-III (*11*). The phase boundary between CO_2-I and CO_2-III is not well understood. For example, Raman studies were presented that showed the stability of CO_2-III to be above 18 to 20 GPa [R. C. Hanson and L. H. Jones, *J. Chem. Phys.* **75**, 1102 (1981)], whereas the x-ray study determined the structure of CO_2-III as occurring at 10 GPa. The structure and existence of CO_2-II and CO_2-IV are still not characterized.
8. We observed a large pressure gradient of CO_2 that exceeds 10 to 20% of its maximum pressure between 10 and 70 GPa at ambient temperature, which ranges from 10 to 20 GPa over a typical sample size of 100 μm in diameter. Such an unusually large pressure gradient has also been observed by others [R. C. Hanson, *J. Phys. Chem.* **89**, 4499 (1985); (*11*)]. In fact, our Raman studies show that CO_2-I and CO_2-III coexist over a large pressure region, causing some complication in understanding the exact nature of the phase stability and boundary of CO_2-I, CO_2-III, and CO_2-IV, mentioned above in (*7*). Our x-ray data also show the broad nature of the diffraction pattern of CO_2-III above 30 GPa, which is probably due to the large pressure gradient and the increase in materials strength at these pressures.
9. C. S. Yoo, J. Akella, H. Cynn, M. F. Nicol, *Phys. Rev. B* **56**, 149 (1997).
10. In this study, we measured the radiance of the SH emission; for example, the radiance measured at 527 nm is $\sim$10 mW sr^{-1} mm^{-2} nm^{-1} at the expense of the total input laser power of 10 to 20 W at 1054 nm. This translates to $\sim$20 mW of radiation at the sample or 0.1% conversion. Considering the fact that much of the primary input laser light is also consumed for heating the sample, we consider this conversion efficiency as a lower bound.
11. H. Olijnyk and A. P. Jephcoat, *Phys. Rev. B* **57**, 879 (1998).
12. The correspondence between the mode frequencies for the two structures was estimated by considering the ratio of the reduced vibrational masses for the symmetric stretching modes in singly bonded C–O–C and Si–O–Si structures. The angle between the two X–O single bonds was chosen to match the α-quartz

bond angle (104.6°). The low-frequency limit (398 cm^{-1}) results from the consideration of isolated structures (X_2O molecules), whereas the high-frequency limit (491 cm^{-1}) results from the consideration of the second-order shell of O atoms moving rigidly with C (Si).

13. R. J. Hemley, in *High Pressure Research in Mineral Physics*, M. H. Manghnani and Y. Syono, Eds. (Terra Scientific, Tokyo, 1987), pp. 347–359.
14. S. K. Sharma, J. F. Mammone, M. F. Nicol, *Nature* **292**, 140 (1981).
15. J. D. Jorgensen, *J. Appl. Phys.* **49**, 5473 (1973).
16. T. J. Driscoll and N. M. Lawandy, *J. Opt. Soc. Am.* **B11**, 355 (1994).
17. Y. Sasaki and Y. Ohmori, *Appl. Phys. Lett.* **39**, 466 (1981).
18. In general, the SH of light is generated in noncentrosymmetric crystals, whereas only odd harmonics are observed in centrosymmetric crystals. This stems from the second-order polarization dependence of electromagnetic transitions. In crystals having a center of symmetry, the inversion of all coordinates must leave all relations between physical quantities unchanged. Because the electric field **E** is odd under inversion operations, the polarization field **P** must also be odd, and the coefficients of all even powers in the expansion of the polarization $\mathbf{P} = \varepsilon_o\chi_1\mathbf{E}\sin(\omega t) + \varepsilon_o\chi_2\mathbf{E}^2\sin^2(\omega t) + \varepsilon_o\chi_3\mathbf{E}^3\sin^3(\omega t) + \ldots$ must be 0; ε_o, dielectric constant at ambient conditions; χ, polarizability tensor for medium; ω, frequency of incident light; and t, time. In such crystals, only odd multiples of the incident frequency can be generated.
19. R. W. G. Wyckoff, *Crystal Structures* (Interscience, New York, ed. 2, 1963), vol. 1.
20. S. M. Stishov and V. Popova, *Geochem. Engl. Transl.* **10**, 923 (1961).
21. R. Span and W. Wagner, *J. Phys. Chem. Ref. Data* **25**, 1509 (1996), and references therein.
22. We thank K. Visbeck for experimental assistance and A. McMahan, C. Mailhiot, and M. Nicol for discussions that were valuable to this study. Our x-ray studies were done at the Stanford Synchrotron Radiation Laboratory. This work has been supported by the Laboratory-Directed Research and Development program at the Lawrence Livermore National Laboratory under the auspices of the U.S. Department of Energy under contract W-7405-ENG-48.

23 November 1998; accepted 27 January 1999

Electrostatic Deflections and Electromechanical Resonances of Carbon Nanotubes

Philippe Poncharal,[1] Z. L. Wang,[2] Daniel Ugarte,[3]
Walt A. de Heer[1]*

Static and dynamic mechanical deflections were electrically induced in cantilevered, multiwalled carbon nanotubes in a transmission electron microscope. The nanotubes were resonantly excited at the fundamental frequency and higher harmonics as revealed by their deflected contours, which correspond closely to those determined for cantilevered elastic beams. The elastic bending modulus as a function of diameter was found to decrease sharply (from about 1 to 0.1 terapascals) with increasing diameter (from 8 to 40 nanometers), which indicates a crossover from a uniform elastic mode to an elastic mode that involves wavelike distortions in the nanotube. The quality factors of the resonances are on the order of 500. The methods developed here have been applied to a nanobalance for nanoscopic particles and also to a Kelvin probe based on nanotubes.

Ever since their discovery (*1*), carbon nanotubes have been recognized as particularly important nanoscopic systems (*2–9*). The mechanical properties of carbon nanotubes have been the subject of numerous studies (*10–21*). In several experimental studies, the Young's modulus E was found to be extremely high, on the order of 1 TPa (*12*, *14*, *16*, *21*). Theory appears to confirm this value (*10*, *11*, *22*, *23*), which is on the same order as the elastic modulus along the basal plane of highly oriented pyrolythic graphite: $E_a = 1.06$ TPa (*24*). Recent determinations of the Young's modulus rely primarily on rigidity measurements (*25*) and assume that the nanotubes bend by uniform compression of the inner arc of the bent tube and uniform elongation of the outer arc, as for an isotropic rod (*10*). Those measurements either involved electron microscopy–based measurements of thermal vibration amplitudes (*12*) or atomic force microscope (AFM) measurements of cantilevered (*16*) or otherwise suspended (*21*) nanotubes. The arc-produced carbon nanotubes with diameters up to $D = 76$ nm were all found to be rigid, with Young's moduli in the terapascal range. The measurements made to date suffer somewhat from experimental uncertainties such as precise measurements of the thermal vibrational amplitudes, the effect of the AFM tip on the nanotubes, and calibration of the AFM cantilever. Furthermore, they do not give information on the damping of vibrations nor on the shapes of stressed nanotubes.

Here we introduce methods for investigating properties of carbon nanotubes that may be extended into the mesoscopic size range. We used those methods on arc-produced, multiwalled carbon nanotubes (MWNTs) (*26*). The technique relies on resonant excitation of selected carbon nanotubes in situ in a transmission electron microscope (TEM) (*27*). In these experiments, we attached a fiber composed of carbon nanotubes (which was recovered from the nanotube arc deposit) to a fine gold wire (*7*). The wire was mounted on a small electrically insulated support so that a potential could be applied to it. This assembly was inserted in a custom-built specimen holder of the TEM in such a way that the fiber was about 5 to 20 μm away from a grounded counterelectrode. The specimen holder was provided with a piezo-driven translation stage and a micrometer-driven translation stage to accurately position the fiber relative to the counterelectrode. To accurately measure the length L and diameter D of the investigated nanotube, the sample holder could be rotated about its axis so that the nanotube under investigation could be aligned perpendicular to the electron beam.

When a static potential V_s was applied to the wire, the carbon nanotubes that protruded from the fiber became electrically charged and were attracted to the counterelectrode. The nanotubes that were not perpendicular to the counterelectrode bent toward it (Fig. 1). We compared the shape of the bent nanotube to that of a cantilevered elastic beam when a force was applied to its tip and also to that of a beam with a uniformly distributed force. This analysis demonstrated that the force exerted on the nanotube is essentially entirely at the tip, hence the charge should be located there. [This result is expected from classical electrostatics applied to conducting needle-shaped conductors (*28*).] Furthermore, the measured deflection is proportional to V_s^2 [after taking into account a slight voltage offset (Fig. 1C)]. This is to be expected for a nanotube that follows Hook's law, because the force equals the product of the induced electric charge (proportional to V_s) and the electric field (also proportional to V_s). Hence, if the charge on the tip equals αV_s, where α is a nanotube-dependent constant that depends on the geometry, and if the electric field is βV_s, then the static force at the tip is $F_s = \alpha\beta V_s^2$. Small deflections are proportional to F_s. In the course of these measurements, we found that a nanotube with $D = 20$ nm can be bent to a radius of curvature at least as small as 80 nm, after which it returns to its original straight configuration, which indicates that such extreme bending does not exceed the elastic limit (*14*, *19*).

Application of a time (t)-dependent voltage to the nanotubes [$V(t) = V_d\cos(\omega t)$]

---

[1] School of Physics, Georgia Institute of Technology, Atlanta, GA 30332–0430, USA. [2] School of Materials Science and Engineering, Georgia Institute of Technology, Atlanta, GA 30332–0245, USA. [3] Laboratório National de Luz Síncrotron, Cx Postal 6192, 13083–970 Campinas SP, Brazil.

*To whom correspondence should be addressed.